Ballistic propagation of density correlations and excess wall forces in quenched granular media

Thomas Schindler [*]

Theoretische Physik 1, FAU Erlangen-Nürnberg, 91058 Erlangen, Germany

Christian M. Rohwer [†]

Department of Mathematics and Applied Mathematics, University of Cape Town, 7701 Rondebosch, Cape Town, South Africa;
Max Planck Institute for Intelligent Systems, 70569 Stuttgart, Germany;
and 4th Institute for Theoretical Physics, University of Stuttgart, 70569 Stuttgart, Germany

We investigate a granular gas in a shaken quasi-two-dimensional box in molecular dynamics computer simulations. After a sudden change (quench) of the shaking amplitude, transient density correlations are observed orders of magnitude beyond the steady-state correlation length scale. Propagation of the correlations is ballistic, in contrast to recently investigated quenches of Brownian particles that show diffusive propagation [Rohwer *et al.*, Phys. Rev. Lett. **118**, 015702 (2017), Rohwer *et al.*, Phys. Rev. E **97**, 032125 (2018)]. At sufficiently strong cooling of the fluid the effect is overlaid by clustering instability of the homogeneous cooling state with different scaling behavior. We are able to identify different quench regimes. In each regime correlations exhibit remarkably universal position dependence. In simulations performed with side walls we find confinement effects for temperature and pressure in steady-state simulations and an additional transient wall pressure contribution when changing the shaking amplitude. The transient contribution is ascribed to enhanced relaxation of the fluid in the presence of walls. From incompatible scaling behavior we conclude that the observed effects with and without side walls constitute distinct phenomena.

I. INTRODUCTION

A dynamic system of macroscopic particles tends to dissipate kinetic energy due to inelastic collisions. In order to maintain particle motion, energy input by an external source is needed. One of the setups commonly employed to this end is the quasi-two-dimensional (2D) granular shaker, which consists of a flat box filled with typically millimeter-sized beads (usually made of metal or glass), that is vibrated vertically. The directed energy input is randomized in particle-particle collisions yielding dynamical steady states reminiscent of thermal equilibrium. In particular, the parameter space for formation of regular lattices, fluids, and coexistence thereof [1–8] bears analogy to the corresponding 2D equilibrium system [9]. However, several properties reveal the nonequilibrium nature of the steady states, such as inelastic collapse at the bottom of the container [10–13], inhomogeneous granular temperatures [1,14], non-Gaussian velocity distributions [15–17], segregation of mixtures [6,18,19], and inelastic hydrodynamic modes [20]. Additionally, granular systems are known to exhibit nonequilibrium collective phenomena such as flocking [21] and pattern formation [22].

In the present study we disturb the steady state by changing the driving strength in order to search for further evidence of its nonequilibrium origin. This technique has proven fruitful

as several anomalies in response functions have been reported, e.g., in the Kovacs memory effect [23–25] or in the compaction behavior [26–29]. Our concrete goal is to illustrate the emergence of collective phenomena (i.e., transient correlations on large scales) that reveal how nonequilibrium states of driving and dissipation are fundamentally different from thermal equilibrium—a fact that is disguised by the phenomenological resemblance of the steady states. We go about this by analyzing the structure of correlations emerging after a change in the vibration amplitude. Additionally, we study the differences to Brownian dynamics following quenches, in which similar correlations have been reported [30,31], in order to uncover the origin of the observed effects.

Part of the article is devoted to classical Casimir forces [32] between distant walls, mediated by the granular medium. The term is borrowed from the corresponding quantum effect [33] related to fluctuating electromagnetic fields confined in a two-plate geometry (Casimir geometry).

When the properties of the medium are altered by the confinement, either through a modification of the fluctuation modes of the medium (fluctuation induced) or by an alteration of the fluid density (density induced), this can result in nontrivial macroscopic forces between the confining surfaces [34–38]. Both effects have been demonstrated in the Brownian reference system. The question addressed in this article is whether the shaken granulates also exhibit such forces and whether these can be classified as either fluctuation induced or density induced.

---
[*]thomas.schindler@fau.de
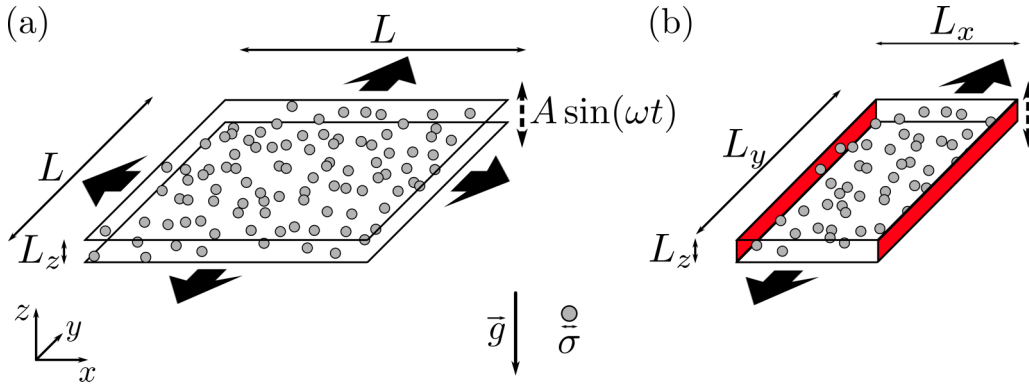[†]christian.rohwer@uct.ac.za

FIG. 1. Sketches of the setup (a) in bulk geometry and (b) with side walls (red) confining the simulation box in the x direction. The bold arrows indicate the directions in which periodic boundary conditions are applied. Dashed arrows mark the shaking in z direction. Symbols are declared in the main text.

The paper is organized as follows. In Sec. II we introduce the examined setup and give technical details about simulation parameters. Our results for density correlations in bulk simulations are presented in Sec. III. We observe large-scale correlations after a change in driving amplitude, for which we carve out similarities and differences to Brownian dynamics. Section IV treats temperature and pressure in a geometry with additional side walls, and discusses their finite-size scaling in steady state and after quenches. In Sec. V we conclude by classifying the observed phenomena.

II. SETUP AND MODEL

We consider a system of N hard spheres of diameter σ and mass m_p in a shallow cuboidal box with dimensions $L_x \times L_y \times L_z$ ($L_z = 2\sigma$) with hard bottom and top plates (see Fig. 1). Gravitational acceleration g acts in the negative z direction, which induces a timescale $\tau_0 \equiv \sqrt{\sigma/g}$ and an energy scale $\epsilon \equiv m_p g \sigma$. The two plates are oscillating in phase with a time-dependent displacement in the z direction and their vertical positions are described by $\pm L_z/2 + A \sin(\omega t + \varphi)$ with an amplitude A, an angular frequency $\omega = 50\tau_0^{-1}$, time t, and a phase shift φ. The sole purpose of introducing φ here is to clarify that quenches (explained below) are not in sync with the plate oscillation; this is achieved by averaging over φ. The area density of particles is fixed to $\rho \equiv N/L_x L_y = 0.5\sigma^{-2}$ throughout the paper.

The main control parameter in this article is A, and three different amplitudes, $A_1 \equiv 0.002\sigma$, $A_2 \equiv 0.005\sigma$, and $A_3 \equiv 0.05\sigma$, are considered. We conduct steady-state simulations at constant A, as well as quenched simulations. Quenches are performed by suddenly increasing or decreasing the shaking amplitude at $t = 0$ from an initial value A_I to a final value A_F and observing the granular fluid after the quench. Henceforth we denote quench protocols between A_1 and A_2 as "moderate quenches" and protocols starting from or ending at A_3 (with A_3 being an order of magnitude larger than A_1 and A_2) as "strong quenches." As the setup is very shallow, we treat it as an effective 2D system and calculate observables only from the x and y components of particle positions and velocities.

Two different geometries are investigated. On the one hand, we employ the described setup with periodic boundary conditions in the x and y directions [see Fig. 1(a)], henceforth referred to as (2D) bulk. The lateral box dimensions here are square shaped, with $L \equiv L_x = L_y$ ranging from 100σ to 400σ. The other setup considered has periodic boundary conditions in the y direction (with $L_y = 400\sigma$) but is confined between two vertical immovable side walls in the x direction, separated by a distance L_x ranging from 5σ to 200σ [Fig. 1(b)]. Beyond the side walls we assume an additional infinitely extended exterior domain (not shown) with the same filling density, as would be present in the well-known Casimir setup of two planar walls at finite distance immersed in bulk. The exterior cannot be simulated explicitly due to its infinite size. Instead, we extrapolate simulation results of the interior (obtained for the different L_x) to ∞ in order to emulate the exterior. The main goal here is the measurement of finite-size deviations (from the limit $L_x \to \infty$) in temperature and pressure as differences between the actually simulated interior region and the extrapolated exterior.

The setup is studied in event driven molecular dynamics computer simulations with the DynamO [39] package. The central idea of the algorithm is to predict collisions of particles from their current positions and velocities. These are entered into a schedule. The system is then evolved by forwarding to the next collision in the schedule and calculating the new velocities and the next collisions of the collision partners. The algorithm is suitable for a system with short interaction times and parabolic trajectories in between, such as the hard macroscopic marbles studied here. The interactions are modeled as instantaneous billiard-like collisions with momentum conservation [40]. Energy loss is accounted for by rescaling the relative particle velocities after collisions (either with other particles or with walls) by a coefficient of restitution of 0.95. Coulomb friction (i.e., friction due to relative tangential motion at contact) is neglected, and hence there is no transfer of angular momentum. Therefore, we do not need to simulate rotations of the spheres. While this model is simplistic, it captures the essential mechanisms of energy input and dissipation, and thus creates the nonequilibrium steady states that are also found in experiments or more sophisticated simulations. In our previous studies [8] we found the phase behavior to be consistent with simulations employing rotating spheres [1–7].

III. QUENCHED BULK

In this section we characterize the bulk system [see Fig. 1(a)] after a quench and show how large-scale transient correlations emerge.

A. Global observables and density inhomogeneity

At first, however, we look at the granular temperature and internal mechanical pressure, defined as

$$T \equiv \left\langle \frac{1}{Nd} \sum_{i=1}^{N} \frac{m_p}{2} \mathbf{v}_i^2 \right\rangle \tag{1}$$

and

$$P_{\text{int}} \equiv \left\langle \frac{1}{dL_x L_y \Delta t} \sum_{\text{PP}} \Delta \mathbf{p}_i \cdot (\mathbf{r}_i - \mathbf{r}_j) \right\rangle, \tag{2}$$

respectively. Here $\mathbf{v}_i$ is the velocity of particle i, $d = 2$ is the spatial dimension, PP indicates summation over all particle-particle collisions between particles i and j during a time interval Δt, $\Delta \mathbf{p}_i$ is the change of momentum of particle i during the collision, and $\mathbf{r}_i$ is its position. Angular brackets in both equations denote averages over a large time interval in steady-state simulations or over a small time interval $[t - \Delta t/2, t + \Delta t/2]$ and multiple quench realizations in quenched simulations. We stress once more that all vectors in the above equations are 2D projections onto the xy plane.

Figure 2 shows the two quantities defined in Eqs. (1) and (2) as functions of time t after the quench for several A_I and A_F. We observe two qualitatively different types of behaviors. In the case of heating or moderate cooling ($A_2 \rightarrow A_1$), T and P_{int} relax exponentially in time toward the final steady-state values T_F and $P_{\text{int},F}$, respectively. The relaxation time is inversely proportional to A_F, since A_F is proportional to the root mean square particle velocity. This proportionality is not necessarily true in general but it does apply in the strong shaking regime ($A\omega^2 \gg g$) employed in this work. Here ω provides the predominant timescale (see, e.g., Refs. [2,6]) and therefore the particle velocities scale with the peak velocity of the plates, $A\omega$. Heating protocols exhibit an additional start-up phase of slow temperature and pressure change. The reason for this is the two-step process in which energy is transferred in particle-plate collisions to the vertical degrees of freedom at first and to the horizontal degrees of freedom only in secondary particle-particle collisions. In contrast, cooling protocols lack the start-up phase, as dissipation takes place homogeneously in every collision.

Only in the case of strong cooling (i.e., with initial amplitude A_3) do T and P_{int} relax algebraically in time. This behavior is known for a freely cooling granular gas [41] which is comparable to the present situation as long as $T(t) \gg T_F$.

The asymmetry between strong heating and strong cooling originates from the asymmetry of energy gain and dissipation of the horizontal degrees of freedom via particle-particle collisions. Cooling through inelastic dissipation takes place in every collision. Heating of the horizontal directions, on the other hand, only occurs, if a particle has been accelerated by the oscillating plates and then transfers its energy to horizontal motion in a particle-particle collision as has been demon-
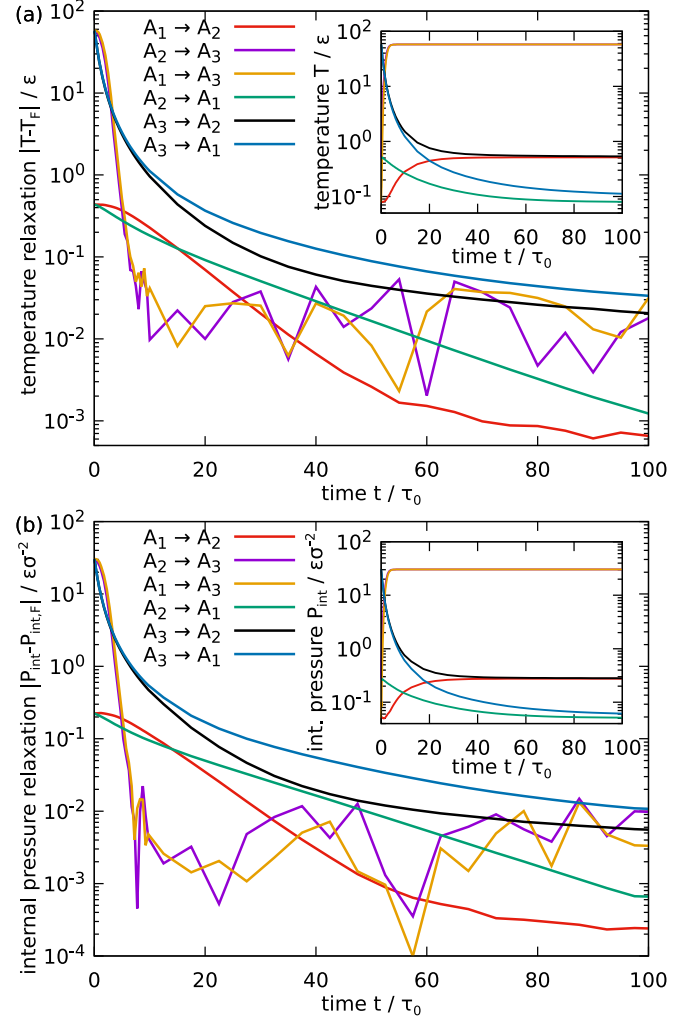

FIG. 2. (a) Relaxation of the temperature T toward the final steady-state value T_F in the quenched fluid as a function of time t after the quench on logarithmic scale for several initial and final amplitudes A_i ($i = 1, 2, 3$) as indicated. The insets show the values of T itself. The T_F at each A_i are obtained in separate steady-state simulations. Panel (b) shows the same analysis as (a) but for the internal pressure P_{int}. Data for $A_F = A_3$ (orange and purple lines) at $t > 7\tau_0$ display noise which is proportional to the higher values of T_F or $P_{\text{int},F}$, respectively.

strated for steady-state fluctuations in a setup with particles of differing masses [18,19]. Moderate quenches constitute only weak disturbances of the steady state where the described asymmetry plays only a minor role. As we shall see, the two described cases are distinct by other observables as well. Hence, we will refer to heating or moderate cooling as type I and to strong cooling as type II behavior in the remainder of the paper.

The different types can even be distinguished when comparing simulation snapshots by eye. Figure 3 shows two different time series, where the particle color encodes the local density. In the type I simulation (top row) the system remains homogeneous and only the distribution of local densities of the particles becomes more heterogeneous with increasing T, which can be seen by the number of small dense patches
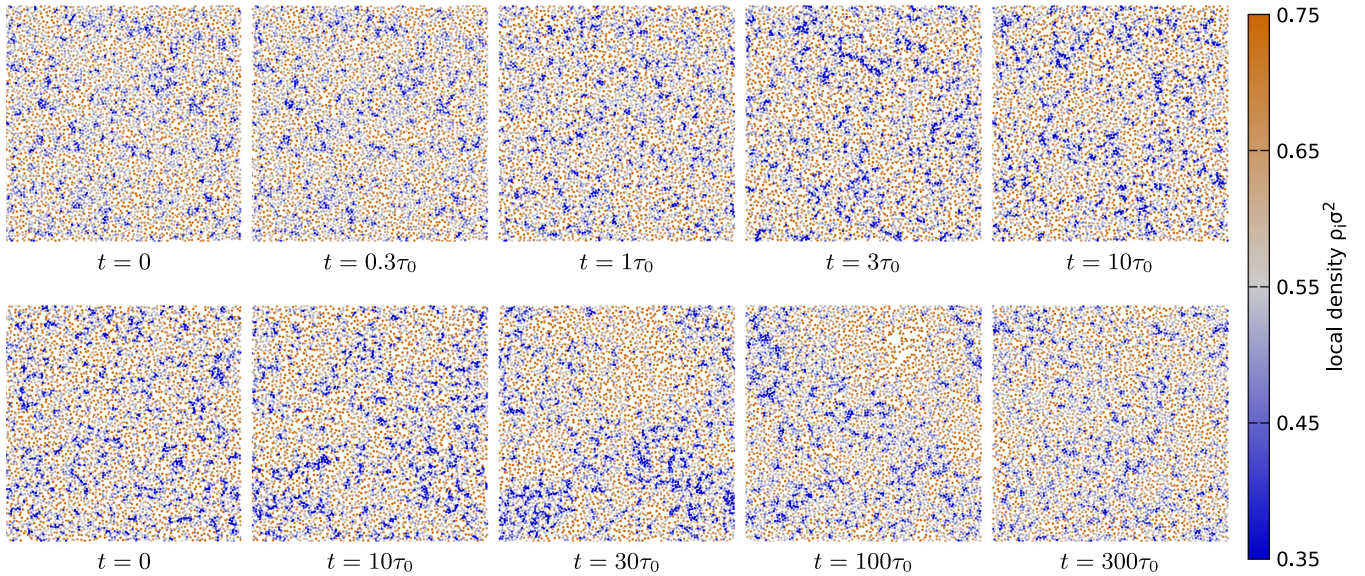
FIG. 3. Time series of top view simulation snapshots. Top row: Strong heating from $A_1 \rightarrow A_3$ (type I). Bottom row: Strong cooling from $A_3 \rightarrow A_1$ (type II). Amplitude change takes place at $t = 0$. The color of each particle i encodes its local density ρ_i as depicted in the color bar. We calculate ρ_i as the inverse area of its 2D Voronoi cell [42], which is the set of points closer to particle i than to any other particle.

increasing. This is a consequence of faster particles exploring the upper half of the box and hence displaying larger overlaps in projection (cf. Appendix). The bottom row shows the reverse process of strong cooling and has switched initial and final states. At intermediate times, however, we observe the formation of dense and dilute domains on the scale of the box size. (See, e.g., the diluted region in the upper right part in the snapshots of $t = 30\tau_0$ and $100\tau_0$.) This constitutes a clustering instability (see, e.g., Refs. [43,44]) which is ultimately dissolved by the weak shaking at A_F. The clustering instability is not necessarily but commonly observed in free cooling states. It therefore serves as an indicator of free cooling, and nicely illustrates the asymmetry between cooling and heating discussed before.

B. Large-scale correlations

Now we turn to two point correlations measured by the transient total correlation function [45]

$$h(r, t) \equiv \left\langle \frac{1}{\rho^2} \sum_{i=1}^{N} \sum_{j \neq i}^{N} \delta(\mathbf{r}_i - \mathbf{r}) \delta(\mathbf{r}_j - \mathbf{r}') \right\rangle - 1, \quad (3)$$

where δ is the Dirac delta distribution, $\mathbf{r}$ and $\mathbf{r}'$ are two 2D position vectors, and $r \equiv |\mathbf{r} - \mathbf{r}'|$. Figure 4 shows time series of h as a function of r for all considered quench protocols. In the range $r < 5\sigma$ there are exponentially decaying oscillations (off scale), which constitute the fluid structure also present in the steady state [cf. Fig. 11(b)]. The focus of this work is not this well-known feature of any dense liquid [45] but rather the transient contributions that are observed at larger distances $r > 5\sigma$.

In the initial state $t = 0$ (black curves) there are no large-scale correlations. After the quench, however, these build up in time and decay to zero again as $t \rightarrow \infty$. There are two rather distinct types of behaviors for type I and II protocols as

classified in Sec. III A. In type I simulations [Fig. 4(a)–4(d)] we find oscillating correlations with local maxima and/or minima. (The monotony is discussed in Sec. III D.) The extrema are propagating in time toward $r \rightarrow \infty$ and are of the order of at most $\sim 10^{-3}$ in magnitude. The shape of each function does not exhibit finite-size scaling, i.e., it is stable against utilizing different box sizes (aside from boundary effects at $r \approx L/2$). Type II protocols [Figs. 4(e) and 4(f)] exhibit larger correlations up to 10^{-2} in magnitude that are not propagating and are positive in sign. The fact that the correlations do not vanish for $r \rightarrow L/2$, but approach a small negative value, indicates density inhomogeneities at the scale of the box size, and clearly constitutes a finite-size effect. This confirms the conclusions from the inspection of the snapshots and characterization of type II behavior as inelastic collapse.

The remainder of the section is devoted to quantitative evaluation of the type I behavior via the length and magnitude of the correlations. The correlation length r_E is measured in terms of the positions of the rightmost local extrema [marked with black crosses in Figs. 4(a)–4(d)]. Figure 5(a) shows the r_E as functions of t. We identify two distinct regimes, namely a short-time regime during which T still adjusts to A_F (cf. Fig. 2), and a long-time regime at constant T. In the short-time regime, the propagation velocity v_E of the extremum increases or decreases as T increases or decreases in heating or cooling protocols (cf. Fig. 2). As T relaxes to the final steady-state value, v_E takes a constant value approximately proportional to A_F, which lies in the range

$$v_E = (11.4 \pm 0.5) A_F \omega \quad (4)$$

for the different protocols. Hence we obtain the dynamic scaling exponent $\alpha = 1$ (defined via $r_E \propto t^\alpha$) of ballistic motion.

A physical interpretation of v_E could be provided by the following possible origin of the correlations, which—in the case of heating—is similar to bursts caused by collisions
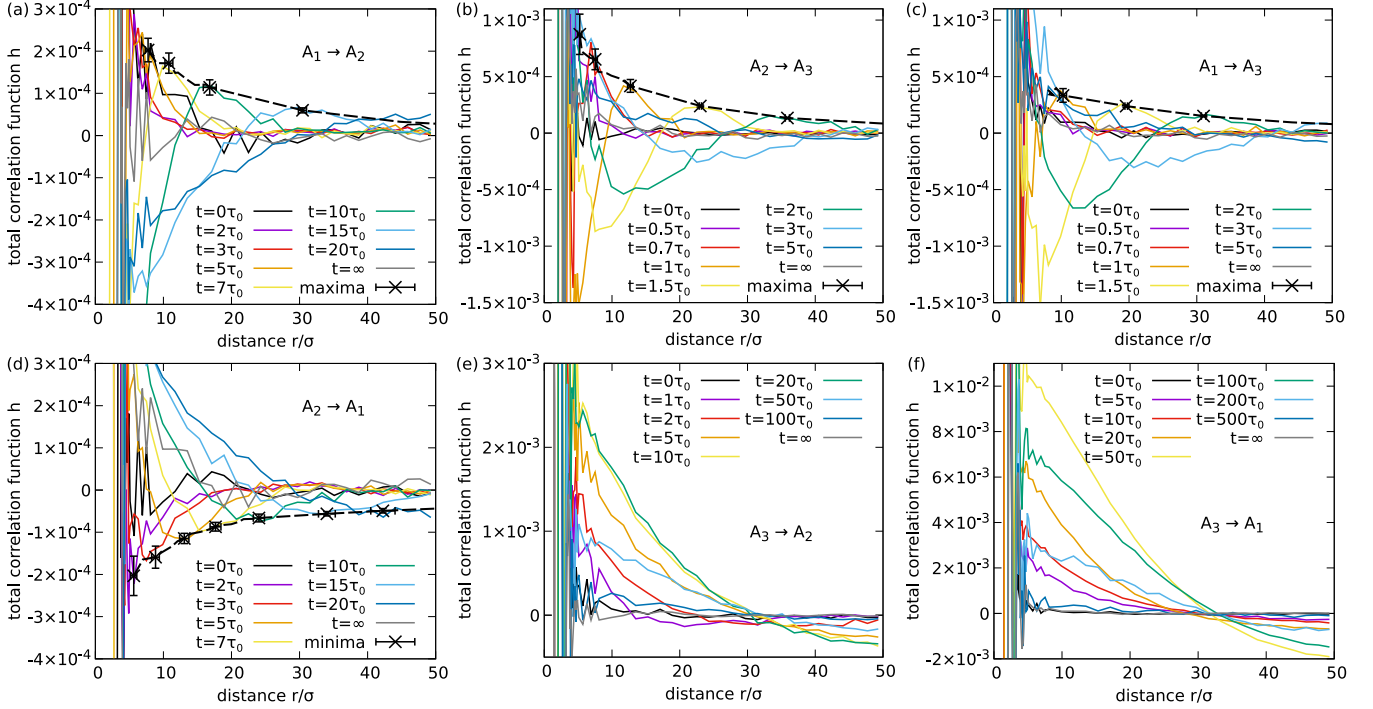
FIG. 4. Total correlation function h as a function of distance r, obtained with box size $L = 100\sigma$ at a selection of times t as indicated. A small value of $5 \times 10^{-5} = 0.25/N$ has been added to the data to correct the usual $\mathcal{O}(1/N)$ finite-size effect of two point correlation functions [45] such that $h(L/2, 0) = 0$. Top row panels [(a)–(c)] show heating protocols, and bottom row panels [(d)–(f)] show cooling protocols. The left column [(a) and (d)] shows quenches between A_1 and A_2 (moderate), the middle column [(b) and (e)] between A_2 and A_3 (strong), and the right column [(c) and (f)] between A_1 and A_3 (strong). Black crosses in type I quenches [(a)–(d)] mark the rightmost local extrema (r_E, h_E) at the shown t, extracted from quadratic polynomial fits of $h(r)$ to that region. The correlation length r_E and the magnitude $h_E \equiv h(r_E)$ of correlations extracted in this manner are utilized in our subsequent analysis. Dashed black lines connect fitted extrema of all t [also of t for which the $h(r)$ are not shown].

of heavy particles reported in Ref. [19]. On heating (weak cooling), particles are accelerated (decelerated) in the z direction by the oscillating plates to a velocity $\propto A_F\omega$. Accelerated (decelerated) particles may transfer their kinetic energy to (recover vertical kinetic energy from) horizontal directions in particle-particle collisions, which creates pairs of excess (depleted) momenta in opposite directions of the involved particles. These pairs of momenta induce particle currents, which create correlations that are transported through the granular medium. In this manner, momentum is transferred without loss to other particles, as momentum is conserved in collisions. The propagation speed in the long-time limit (i.e., at saturated temperature) can be estimated as the mean velocity $v_T \equiv \sqrt{T_F/m_p}$ of particles, plus a contribution of the distance covered while momentum is passed on in collisions,

$$v_E \approx v_T + sr_c. \tag{5}$$

Here s is the mean projected distance of colliding particles and r_c is the rate of particle-particle collisions. In steady-state simulations we measured values in the ranges of v_T from $2.8A_F\omega$ to $3.0A_F\omega$ and of r_c from $9.3A_F\omega/\sigma$ to $10.7A_F\omega/\sigma$ for the considered amplitudes. s has not been sampled explicitly but can be calculated from the other quantities to be in the range from 0.82σ to 0.93σ, which is reasonable in this quasi-2D setup. In the intermediate regime the velocity may be reduced (enhanced) due to the reduced (enhanced) temperature. This mechanism requires that particles are thermalized at a variety

of rates, which is not given in the case of strong cooling, where $T_F \ll T_I$, which means that plates are practically immovable and energy loss is dominated by particle inelasticity.

We stress that v_E is not the speed of sound c_s of the final steady-state fluid, which we calculated in supplemental steady-state simulations via the dynamic structure factor according to the method described in Ref. [45] as $c_s(A_1) = (7.8 \pm 0.4)A_F\omega$ and $c_s(A_3) = (4.2 \pm 0.2)A_F\omega$. The fact that $c_s \not\propto A_F\omega$ clearly disqualifies the speed of sound as possible interpretation for v_E.

The magnitude h_E of correlations, measured as the value of the correlation function at the extremum [see Fig. 5(b)], also exhibits a crossover like r_E with the same crossover times. In each of the regimes the dynamics is describable by an algebraic scaling. In the short-time regime $h_E \propto r_E^{-0.7}$ and in the long-time regime $h_E \propto r_E^{-2}$ for all protocols, which yields the scaling exponent of the correlation strength $\beta = -2$.

C. Comparison to Brownian dynamics

We now compare our results to diffusive systems for which a theory has recently been developed [30,31] to describe fluctuation induced correlations after instantaneous temperature changes. We stress that we do not apply this theory to the present simulation results expecting quantitative agreement, but rather compare to the analytical results for Brownian systems to detect universalities and system-specific properties.
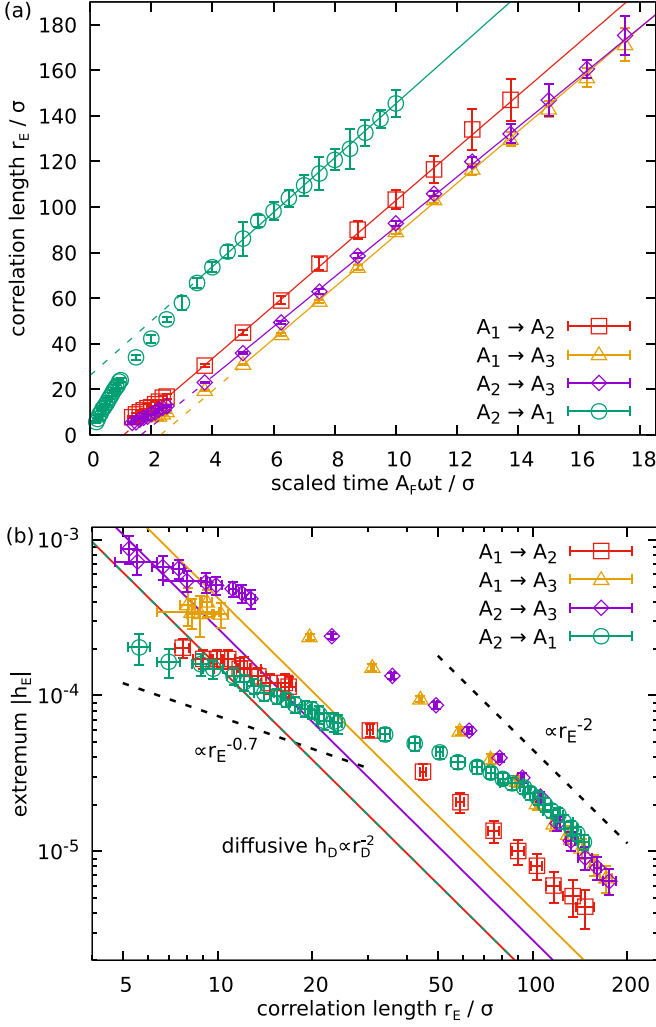
FIG. 5. (a) Correlation length r_E of the total correlation function h as a function of time t (multiplied by the postquench peak velocity of the oscillating plates $A_F\omega$ for comparability), extracted from type I protocols [Figs. 4(a)–4(d)]. Straight lines are linear fits obtained from the data ranges, where the lines are continuous. (b) Absolute values $|h_E|$ of the magnitude of correlations as a function of r_E on double logarithmic scales [same data points as black crosses and dashed lines in Figs. 4(a)–4(d)]. Straight lines are the theoretical predictions $h_D(r_D)$ for diffusive systems with instantaneous temperature quenches according to Eq. (7). The black dashed lines corresponding to power laws with exponents -0.7 and -2 are guides to the eye. Data points of both panels at $r < 50\sigma$ have been obtained in simulation boxes with $L = 100\sigma$, data points at $r > 50\sigma$ have been obtained in simulation boxes with $L = 400\sigma$.

The theory predicts a Gaussian distribution of the correlations,

$$h(r,t) = \frac{S_I - S_F}{\rho} \frac{\exp\left(-\frac{r^2}{2r_D(t)^2}\right)}{\sqrt{2\pi r_D(t)^2}^d}, \qquad (6)$$

where S_I and S_F are the zero-wavelength limits of the static structure factors of the initial and final steady-state fluid, respectively, and r_D is the correlation length. For quantitative comparison, we extract the inflection point of this function, giving us the typical strength and length scale of correlations.

The typical strength is obtained by setting $r = r_D$,

$$h_D(r_D) = \frac{S_I - S_F}{\rho\sqrt{e}2\pi r_D^2} \propto r_D^{-2}. \qquad (7)$$

yielding a scaling exponent $\beta = -2$. Note that this is independent of the dynamical scaling of r_D and only depends on the spatial dimension. Therefore, β can be seen as a geometric property that ensures constant normalization of the Gaussian distribution. The correlation length as a function of time reads

$$r_D(t) = \sqrt{4D_F t} \propto t^{1/2}, \qquad (8)$$

with the long-time single-particle diffusion coefficient D_F of the final steady state. This implies $\alpha = 1/2$—the dynamic scaling exponent of diffusive motion.

The prefactor in Eq. (7) is proportional to the difference of the initial and final steady-state static structure factors, which are connected to the respective compressibilities χ via $S = \rho T \chi \equiv T \partial\rho/\partial P$. Hence, we only expect a nonzero effect for thermal particles with variable softness. In the present setup we employ hard spheres, which are athermal by themselves. As scrutinized in the Appendix, however, we create an effective softness via variation of the stratification of the particles at different A, which influences their overlaps in the 2D projection. This makes it possible to observe the predicted effect in our system despite the hard core model. Note that we use the term "softness" for structural properties of the fluid rather than material properties of the individual particles. Overlaps due to actual compression of glass or metal spheres in experiments or in different simulation models would be orders of magnitude smaller than the overlaps due to stratification.

A first notable observation when comparing our results to the diffusive case, is the rather different functional form of h. While the Brownian theory predicts a universal Gaussian shape of the correlations, we observed a more complicated function shape with oscillating behavior that depends on the applied protocol (see also below). Therefore, we only compare the scaling exponents of the extracted extrema shown in Fig. 5 to Eqs. (7) and (8), and not the prefactors.

Even though the theory is not directly applicable here, the value $\alpha = 1$ obtained in our simulations is remarkable. T is fully relaxed in the long-time regime and thus one could expect the postquench fluid to behave like a steady-state fluid. Indeed, we performed preparatory steady-state simulations where we find diffusive motion of the individual particles for $r > 50\sigma$. However, the correlation function exhibits the ballistic scaling of propagating waves. This confirms the interpretation as a collective phenomenon, in which information is not carried by the individual particles, but transferred between particles in collisions, as proposed previously in Sec. III B.

The picture is quite different when considering β. Here the long-time limit $\beta = -2$ fits the diffusive theory well. This universality supports the notion that β is a purely geometric quantity that is independent of the dynamic details and designates the correlations as a conserved quantity in steady state. The scaling $|h_E| \propto r_E^{-0.7}$ during thermalization, on the other hand, indicates a normalization which increases in time or in other words a source of correlations. This observation supports the picture of a build-up of correlations during temperature equilibration as proposed before.
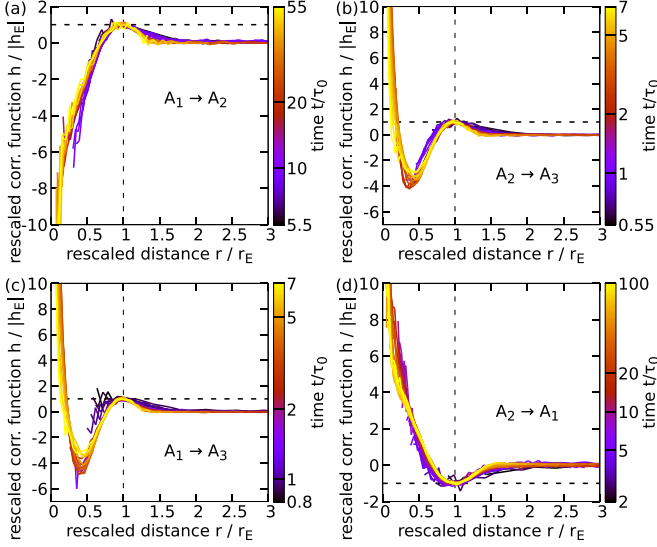
FIG. 6. The same data as Figs. 4(a)–4(d), but with abscissa and ordinate rescaled by correlation length $r_E(t)$ and correlation magnitude $|h_E(t)|$, respectively [such that the extrema collapse at (1,1) or (1,−1)]. Protocols are indicated in the labels. Only data exhibiting an extremum in h is shown. Panels (a) and (b) show moderate heating and cooling, respectively. Panels (c) and (d) show strong heating. Time is encoded in the color of each curve as depicted in the colored bars of the panels.

D. Universal functional shape

In order to characterize its features, we collapse $h(r)$ for different t by rescaling abscissa and ordinate with the values of the extrema, i.e., we plot $h/|h_E|$ versus r/r_E as shown in Figs. 6(a)–6(d) for the different quench protocols. By definition, this scaling function has a local maximum at (1,1) for heating or minimum at (1, −1) for cooling protocols. What is striking here is the stability of the function shapes, which is in sharp contrast to the strong crossover of the scaling exponents. There are only slight shifts of the functions left and right of the main extrema at the times of the crossover.

At moderate heating [Fig. 6(a)] only a single maximum is present. For $r \to 0$, h attains negative values and for $r \to \infty$, h decays toward zero.

The strong heating protocols (b) and (c) both show the same qualitative behavior, which differs from moderate heat-

ing by an additional local minimum at $\approx (0.4, −4)$ before or $\approx (0.5, −3)$ after the crossover. Consequently there is an additional zero at $r/r_E \approx 0.2$ and $h > 0$ for $r \to 0$. This new feature could be attributed to an additional process that only takes place when the fluid temperature is changed strongly. The feature is located at smaller r than the original extremum, indicating that the additional process takes place at a later time than the process that creates the maximum at (1,1). The data, however, does not reveal the nature of this process.

Moderate cooling [Fig. 6(d)] exhibits exactly the same behavior as moderate heating but with the opposite sign. This is a clear signature for a linear response regime.

IV. CASIMIR GEOMETRY

This section treats the setup with side walls as depicted in Fig. 1(b). The aim here is to report boundary effects on global observables and to determine whether these are caused by the bulk postquench correlations described in the previous section as is the case in diffusive systems [30].

We start by describing confinement effects in the steady state by means of T, P_{int}, and the pressure on the side walls,

$$P_{\text{wall}} \equiv \left\langle \frac{1}{2L_y \Delta t} \sum_{\text{PW}} \Delta \mathbf{p}_i \cdot \mathbf{n}_w \right\rangle, \tag{9}$$

where the sum is performed over all particle-wall collisions of any particle i with either of the side walls (with normals $\mathbf{n}_w = \pm \mathbf{e}_x$) during Δt. Figure 7 shows T, P_{int}, and P_{wall} as functions of L_x^{-1}. We observe a linear dependence on L_x^{-1} in all three functions. Extrapolations to $L_x \to \infty$ agree with the values T_{bulk} and P_{bulk} of temperature and internal pressure, respectively, of separate bulk simulations performed beforehand (dashed lines). Linear fitting and averaging over amplitudes yields

$$T(L_x) = T_{\text{bulk}}\left[1 - (0.8 \pm 0.1)\sigma L_x^{-1}\right],$$
$$P_{\text{int}}(L_x) = P_{\text{bulk}}\left[1 - (1.4 \pm 0.1)\sigma L_x^{-1}\right],$$
$$P_{\text{wall}}(L_x) = P_{\text{bulk}}\left[1 + (0.3 \pm 0.1)\sigma L_x^{-1}\right]. \tag{10}$$

[Note that $P_{\text{int}}(L_x)$ and $P_{\text{wall}}(L_x)$ converge to the same value in the limit $L_x \to \infty$.] T decreases with decreasing L_x and P_{int} follows the temperature behavior. P_{wall}, however, increases with decreasing L_x, which constitutes a nontrivial effect: In a
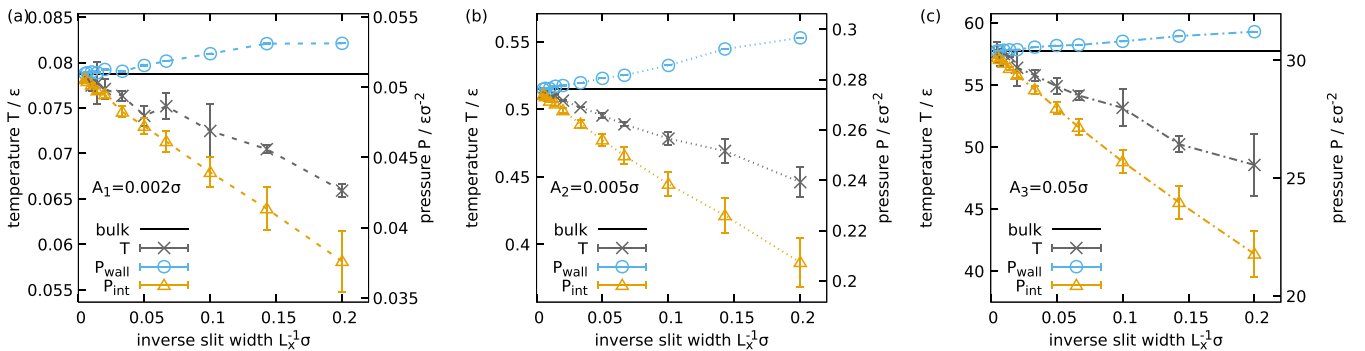

FIG. 7. Temperature T, internal pressure P_{int}, and side wall pressure P_{wall} in the slit geometry as functions of inverse slit width L_x^{-1} at steady state. (a) Amplitude A_1, (b) A_2, and (c) A_3. The temperature scale (left ordinate) and pressure scale (right ordinate) are adjusted such that the origins (off scale) and bulk values of T and P_{int} (marked by straight black lines) coincide. Lines connecting data points are guides to the eye.

setup, where the side walls were placed in an infinite system with fluid both inside and outside the side walls, the exterior domain would exert a side wall pressure of the extrapolated value. Hence, there would be a net *expanding* force on the side walls even though the granular temperature is smaller at the interior. Qualitatively, the finite-size scaling can be described in terms of an excess particle accumulation at the side walls [31] that changes the density between the walls by a contribution $\propto L_x^{-1}$.

Next, we turn to quenches of the Casimir geometry, and investigate whether there is an effect beyond these steady-state confinement effects. The dynamics of T is shown for a type I quench in Fig. 8(a) and a type II quench in Fig. 8(b). As in the bulk setup (cf. Fig. 2), T relaxes to the steady-state value T_F exponentially in the type I quench but algebraically in the type II quench. Other type I quenches between $A_1 \leftrightarrow A_2$ (not shown) also show the same behavior as Fig. 8(a). P_{wall} shown for heating in Fig. 8(c) and cooling in Fig. 8(d) exhibits similar behavior as T. The main difference is the inverted finite-size scaling (i.e., deviation from the limit $L_x \to \infty$) of the initial and final states, which is consistent with the steady-state results (cf. Fig. 7).

The temperature differences ΔT between the exterior and interior [Fig. 8(e) and 8(f)] transition monotonically from the initial to the final steady-state values plotted in Fig. 7(a) and 7(c). The net side wall pressure ΔP_{wall} [Figs. 8(g) and 8(h)], however, shows an undershoot or overshoot in the case of heating or cooling, respectively. The undershoots in the heating simulations [Fig. 8(g)] for all L_x take place at $t \approx 2$–$3\tau_0$, which is roughly the time at which the fluid is fully heated [cf. Fig. 8(a)]. The times $t \approx 1$–$2\tau_0$ of the overshoots at cooling [Fig. 8(h)] coincide with the start of the cooling of the fluid [cf. Fig. 8(b)]. Moderate heating $A_1 \to A_2$ shows the same behavior as strong heating and moderate cooling $A_2 \to A_1$ shows the same behavior as strong cooling (not shown). The extremum is, however, not as pronounced upon moderate amplitude changes. We would like to stress that the qualitative behavior here does not correspond to the types-I and -II classification of the previous section but depends on whether the fluid is cooled or heated.

In general, nonmonotonic behavior of the pressure and temperature may indicate a separation of timescales as regards dynamics in the vicinity of the surfaces and dynamics of the bulk. Overshoots of this type have, e.g., been observed in drift-diffusion systems [46]. To explain the net pressure overshoot in our system, we collapse the data and obtain the finite-size scaling. We assume that the data follows the scaling relation

$$y(t/s_t(L), L) = s_y(L)y(t, \infty) \qquad (11)$$

for all considered observables $y = T, P_{\text{int}}, P_{\text{wall}}$, with scaling factors s_t and s_y describing the scaling of time and of the final steady-state value, respectively. The scaling factors are determined by minimizing an error function defined via

$$E(s_t, s_y) \equiv \frac{1}{t_F} \int_0^{t_F} dt \left[\frac{y(t/s_t, L)}{s_y y(t, \infty)} - 1 \right]^2, \qquad (12)$$

with an upper bound of integration t_F, which is in practice given by the range of simulation data. This error function is defined such that $E = 0$ if Eq. (11) is satisfied and $E > 0$ oth-
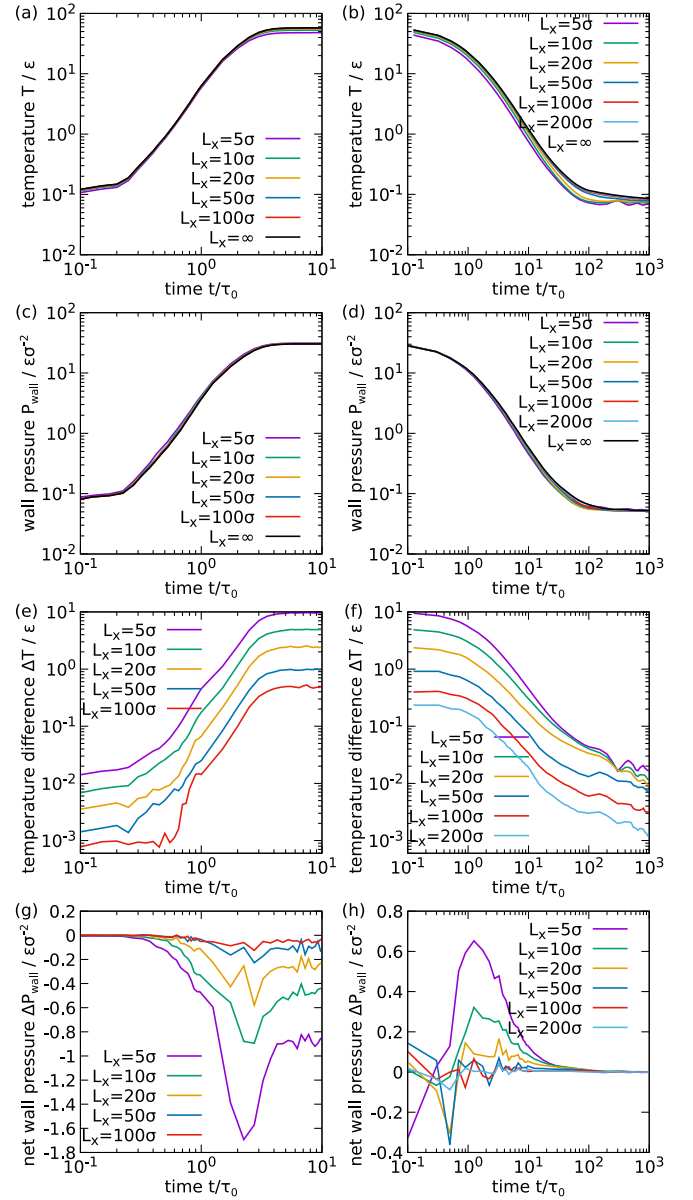

FIG. 8. Data for temperature T and side wall pressure P_{wall} as functions of time t after the quench (logarithmic scale) for several slit widths L_x as indicated in each panel. [(a) and (b)] T on logarithmic scale. [(c) and (d)] P_{wall} on logarithmic scale. [(e) and (f)] Temperature difference $\Delta T \equiv T(\infty) - T(L_x)$ between the exterior and interior of the slit on logarithmic scale. [(g) and (h)] Net side wall pressure $\Delta P_{\text{wall}} \equiv P_{\text{wall}}(\infty) - P_{\text{wall}}(L_x)$ (i.e., difference between pressures on outer and inner surfaces of the side walls). Left column [(a), (c), (e), and (g)]: Strong heating $A_1 \to A_3$ (type I). Right column [(b), (d), (f), and (h)]: Strong cooling $A_3 \to A_1$ (type II). Data for $L_x = \infty$ is extrapolated from finite L_x at each time, as was done for the steady-state values (cf. Fig. 7).

erwise. With the input simulation data for $y(t, L)$ and $y(t, \infty)$ being noisy, the true values of s_t and s_y are the ones that minimize E. These are determined simply by sampling a fine grid in the $s_t s_y$ plane and taking the minimum value. The position of the minimum (s_t, s_y) does not depend on the choice of t_F as long as t_F is greater than the time the fluid needs to relax.
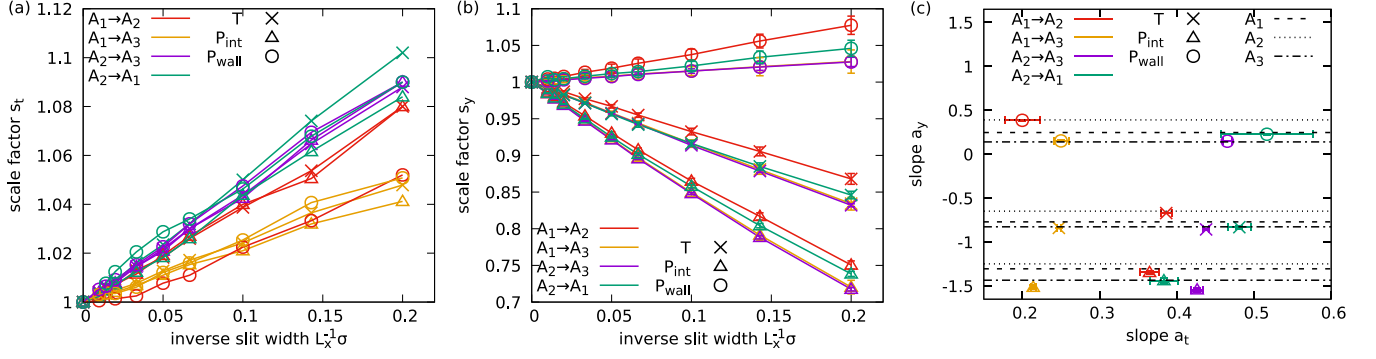
FIG. 9. (a) Scale factor s_t of time as a function of inverse slit width L_x^{-1}. Errors (omitted for clarity) are of magnitude $\sigma_{s_t} = 0.05 L_x^{-1}\sigma - 0.2 L_x^{-1}\sigma$. (b) Same as (a), but for scale factors s_y of the observables $y = T, P_{\text{int}}, P_{\text{wall}}$. Data points for $A_1 \rightarrow A_3$ (yellow) are hardly visible as they mostly coincide with data points for $A_2 \rightarrow A_3$ (purple). Lines in (a) and (b) are guides to the eye. Errors σ_{s_t} and σ_{s_y} are obtained via the criteria $E(s_t, s_y \pm \sigma_{s_y}) \equiv 2E(s_t, s_y)$ and $E(s_t \pm \sigma_{s_t}, s_y) \equiv 2E(s_t, s_y)$. (c) Slopes a_y of linear fits to s_y as functions of the slopes a_t of linear fits to s_t. Lines show the steady-state values of a_y [cf. Eq. (10)] at A_1 (dashed), A_2 (dotted), and A_3 (dashed-dotted). The legends show the encoding of the respective collapsed observables via symbol types, and the quench protocols via colors.

We judge the quality of this numerical data collapse by the minimal value of E being small. This criterion is fulfilled for type I protocols with $E < 0.001 (L_x/\sigma)^{-1}$. For type II protocols, however, we obtain values of up to $E \approx 0.1 (L_x/\sigma)^{-1}$. Therefore, we conclude that the finite-size scaling of cluster instability is not captured adequately by the simple two-parameter scaling of Eq. (11).

Figures 9(a) and 9(b) show s_t and s_y as functions of L_x^{-1}. To a good approximation all scaling factors are linear functions of L_x^{-1} with slopes a_t and a_y plotted against each other in Fig. 9(c). The a_y are equal to our steady-state results in Eq. (10) within the uncertainties (which serves as an additional consistency check for the minimization procedure).

Values for a_t are in the range $0.2 \leqslant a_t \leqslant 0.5$ for the different quench protocols, which implies an enhanced relaxation in the presence of side walls. With this, the nonmonotonic P_{wall}
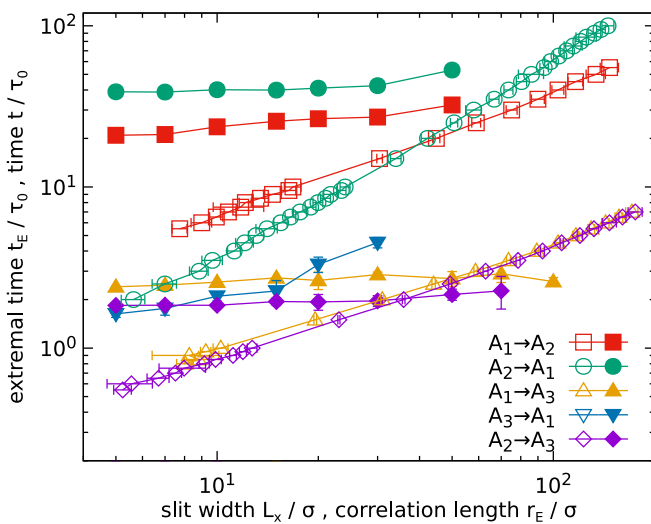

FIG. 10. Extremal times t_E of the side wall pressure under- or overshoots (filled symbols) versus slit width L_x and time t [open symbols; same data as Fig. 5(a)] versus correlation length r_E of the total correlation function h. Same quench protocols are depicted as same symbol shapes and colors. Lines are guides to the eye.

can be explained as follows. The undershoot in the side wall pressure observed when increasing A [Fig. 8(g)] takes place when the fluid between the side walls is already completely heated, while the pressure of the fluid outside is smaller as it is still adjusting to the postquench amplitude. The overshoot in the reverse process [Fig. 8(h)] takes place when the inner fluid has started to cool faster than the fluid outside. The obtained values for the slopes of the scaling factors also explain why the overshoot is not observed in T or P_{int}: Here the overshoot through the enhanced relaxation is overlaid by decreasing of the (initial and final) steady-state values (as $a_t < 0$ and $a_y < 0$ and $|a_y| > |a_t|$ for $y = T, P_{\text{int}}$). The slightly positive value of $a_{P_{\text{wall}}}$, on the other hand, slightly enhances the overshoot.

In order to affirm that the bulk correlations described in Sec. III are not the origin of the transient net pressure overshoot, we compare the dynamic scaling of both effects. To this end, we extract the times t_E at which the extrema of ΔP_{wall} are attained by fitting quadratic functions in the vicinities of the extrema (displayed in Fig. 10). For most protocols t_E increases only slightly with L_x, which does not match the scaling obtained for the bulk correlations (also plotted in Fig. 10). This observation disqualifies the density correlations as origin of the nonmonotonic ΔP_{wall}.

V. DISCUSSION AND CONCLUSION

The quenched granular quasi-2D system considered here exhibits many nontrivial phenomena, several of which were observed when disturbing the steady state by changing the driving amplitude. The first is the emergence of propagating density correlations in bulk on length scales beyond the commonly known fluid structure upon heating or moderate cooling [type I; Figs. 4(a)–4(d)].

Qualitatively such an effect has been predicted recently for soft Brownian particles. However, we identified several crucial differences regarding the dynamic scaling and the functional form of the correlations. An assumption in the previous studies of Brownian systems that is not met by our setup is that of instantaneous temperature change. Here we change the driving amplitude instantaneously and the temperature of

the inertial particles slowly adapts to the new amplitude. This was shown to make an important difference as saturation of the temperature causes a crossover in the scaling behavior (Fig. 5). Remarkably, correlation functions were shown to collapse onto universal position-dependent curves (i.e., scaling functions) when rescaled appropriately (Fig. 6). This universality is robust across different simulation sizes. Although we did not decipher the various features of these curves, we also ascribe their emergence to the gradual temperature change.

In the saturated (i.e., long-time) regime we could identify the scaling of the correlation strength $\beta = -2$ as a universal geometric property. On the other hand, the ballistic scaling of the dynamic exponent $\alpha = 1$ is remarkable because the individual particle motion is diffusive at the considered length scales. For an explanation of the constant propagation speed we proposed a semiquantitative mechanism.

Similar studies of a single event in a granular medium at rest yield an exponent $\alpha = 1/3$ [47]. The momentum there is solely supplied by the initial event and is split among particles, which decreases the propagation speed in time. In contrast, we addressed a medium at nonzero temperature, which is capable of transporting the generated momentum pairs at constant speed. Conclusive verification of the proposed semiquantitative mechanism yet remains an open task for future studies.

The present explanation relies on momentum conservation in horizontal directions. Therefore it is unclear whether the observed correlations are also present in more sophisticated models or experiments that feature tangential friction. Another open puzzle is the determination of the origin of the salient functional forms of the scaling functions. A fruitful path to this end may emerge via the testing of a local conservation law with a possible source term via explicit sampling of particle currents [48].

The asymmetry between energy gain and dissipation induces an asymmetry between heating and cooling. Hence, when cooling the fluid starting from a large A_I we observe an additional effect named clustering instability [type II; Figs. 4(e) and 4(f)]. This effect, which is well known for inelastic systems, is greater and hence overlays the former one. In particular, the true length scale of the clustering instability could not be determined in our simulations, as it exceeded even our largest simulation boxes.

We further investigated the finite-size scaling of temperature and pressure by adding side walls to the setup. While the internal pressure follows the scaling of the temperature, the pressure exerted on the side walls behaves differently. In the steady state, the side wall pressure deviation from the infinite-size limit has the opposite sign than the temperature difference (Fig. 7). Moreover, after a quench we observe nonmonotonic behavior in the side wall pressure (Fig. 8). Numerical data collapse revealed that this is a consequence of an enhanced relaxation speed of the fluid between the side walls (Fig. 9). In combination with the anomalous steady-state behavior, this results in an over- or undershoot in the side wall pressure that is not observed in the temperature or the internal pressure.

The finite-size scaling $\propto L_x^{-1}$ of temperature and pressure as well as relaxation speed corresponds to the fraction of wall size over system area. This is a clear indicator for a change of the bulk properties of the fluid between the walls which

constitutes a density induced effect. Fluctuation induced wall effects on the other hand, which should exhibit the scaling exponent of the bulk correlations $\beta = -2$, were not detected (cf. Fig. 10).

Future plans include investigations of a setup with tuned densities inside and outside the slit such that net side wall pressure in steady state is zero, in order to isolate the transient contribution. A further open question and a possible next objective is the study of forces between compact inclusions immersed in the fluid.

APPENDIX: STEADY-STATE BULK

Here we discuss the steady-state fluid as present in the initial state prior to the quench and in the final state infinitely long time after the quench. The aim is to demonstrate how stratification creates effectively soft particles. Figure 11(a)
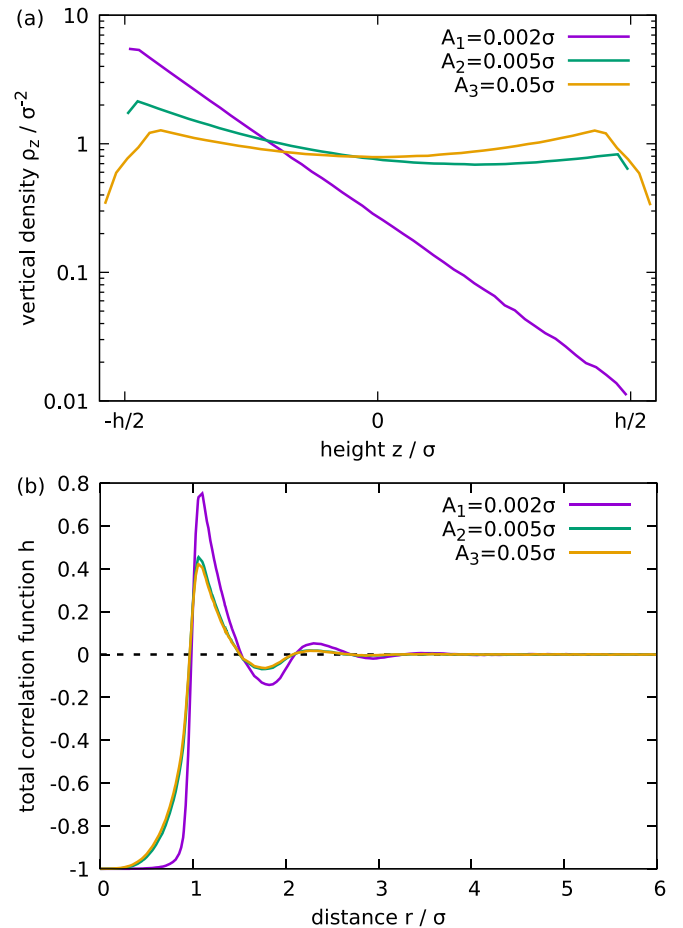

FIG. 11. (a) Vertical density distribution ρ_z as a function of the z coordinate, and (b) projected total correlation function h as a function of distance r, for steady-state fluids at amplitudes A_1, A_2, and A_3.

shows the vertical density distribution

$$\rho_z(z) \equiv \frac{L_z}{L^2}\left\langle \sum_{i=1}^{N} \delta(z_i(t) - z)\right\rangle \qquad (A1)$$

at the three investigated A (normalized such that its mean equals ρ). At high amplitude A_3, ρ_z is almost symmetric and the particles fill the whole space between the plates. The peaks at the top and bottom plates originate from the mutual repulsion of the particles. At low amplitude A_1, however, we observe strongly barometric (i.e., exponentially decaying) distribution of particles, where most particles are located near the bottom plate and are only slightly hop-ping. At intermediate amplitude A_2 the particles are partly stratified.

The differences in stratification also make an impact on h [shown in Fig. 11(b)]. As mentioned before, we obtain h from the projected xy coordinates of the particles. Therefore, even though the particles are hard and cannot penetrate each other, we can observe a nonzero contribution of h at $r < \sigma$ originating from particles that are (partly) on top of each other. This contribution is larger at high amplitudes A_2 and A_3, where particles fill the whole space between the plates, and smaller at low amplitude A_1, where most of the particles populate a single layer near the bottom plate. In a 2D description of the system one can therefore consider the fluid as effectively soft.

[1] A. Prevost, P. Melby, D. A. Egolf, and J. S. Urbach, Phys. Rev. E **70**, 050301(R) (2004).

[2] P. Melby, F. Vega Reyes, A. Prevost, R. Robertson, P. Kumar, D. A. Egolf, and J. S. Urbach, J. Phys.: Condens. Matter **17**, S2689 (2005).

[3] P. M. Reis, R. A. Ingale, and M. D. Shattuck, Phys. Rev. Lett. **96**, 258001 (2006).

[4] M. G. Clerc, P. Cordero, J. Dunstan, K. Huff, N. Mujica, D. Risso, and G. Varas, Nat. Phys. **4**, 249 (2008).

[5] F. Vega Reyes and J. S. Urbach, Phys. Rev. E **78**, 051301 (2008).

[6] N. Rivas, P. Cordero, D. Risso, and R. Soto, New J. Phys. **13**, 055018 (2011).

[7] M. Guzmán and R. Soto, Phys. Rev. E **97**, 012907 (2018).

[8] T. Schindler and S. C. Kapfer, Phys. Rev. E **99**, 022902 (2019).

[9] M. Schmidt and H. Löwen, Phys. Rev. E **55**, 7228 (1997).

[10] J. S. Olafsen and J. S. Urbach, Phys. Rev. Lett. **81**, 4369 (1998).

[11] X. Nie, E. Ben-Naim, and S. Y. Chen, Europhys. Lett. **51**, 679 (2000).

[12] J. S. Olafsen and J. S. Urbach, Phys. Rev. Lett. **95**, 098002 (2005).

[13] E. Khain and I. S. Aranson, Phys. Rev. E **84**, 031308 (2011).

[14] A. E. Lobkovsky, F. Vega Reyes, and J. S. Urbach, Eur. Phys. J.: Spec. Top. **179**, 113 (2009).

[15] W. Losert, D. G. W. Cooper, J. Delour, A. Kudrolli, and J. P. Gollub, Chaos **9**, 682 (1999).

[16] J. S. Olafsen and J. S. Urbach, Phys. Rev. E **60**, R2468 (1999).

[17] A. Kawarada and H. Hayakawa, J. Phys. Soc. Jpn. **73**, 2037 (2004).

[18] N. Rivas, S. Ponce, B. Gallet, D. Risso, R. Soto, P. Cordero, and N. Mujica, Phys. Rev. Lett. **106**, 088001 (2011).

[19] N. Rivas, P. Cordero, D. Risso, and R. Soto, Granul. Matter **14**, 157 (2012).

[20] R. Brito, D. Risso, and R. Soto, Phys. Rev. E **87**, 022209 (2013).

[21] N. Kumar, H. Soni, S. Ramaswamy, and A. K. Sood, Nat. Commun. **5**, 4688 (2014).

[22] I. S. Aranson and L. S. Tsimring, Rev. Mod. Phys. **78**, 641 (2006).

[23] A. Prados and E. Trizac, Phys. Rev. Lett. **112**, 198001 (2014).

[24] E. Trizac and A. Prados, Phys. Rev. E **90**, 012204 (2014).

[25] J. J. Brey, M. I. García de Soria, P. Maynar, and V. Buzón, Phys. Rev. E **90**, 032207 (2014).

[26] M. Nicodemi, Phys. Rev. Lett. **82**, 3734 (1999).

[27] E. Caglioti, V. Loreto, H. J. Herrmann, and M. Nicodemi, Phys. Rev. Lett. **79**, 1575 (1997).

[28] J. J. Brey and A. Prados, Phys. Rev. E **63**, 061301 (2001).

[29] J. J. Brey and A. Prados, J. Phys.: Condens. Matter **14**, 1489 (2002).

[30] C. M. Rohwer, M. Kardar, and M. Krüger, Phys. Rev. Lett. **118**, 015702 (2017).

[31] C. M. Rohwer, A. Solon, M. Kardar, and M. Krüger, Phys. Rev. E **97**, 032125 (2018).

[32] M. Kardar and R. Golestanian, Rev. Mod. Phys. **71**, 1233 (1999).

[33] M. Bordag, G. Klimchitskaya, U. Mohideen, and V. Mostepanenko, *Advances in the Casimir Effect* (Oxford University Press, Oxford, 2009).

[34] G. M. Rodríguez-Liñán, Y. Nahmad-Molinari, and G. Pérez-Ángel, PLoS ONE **11**, e0156153 (2016).

[35] S. Aumaître, C. A. Kruelle, and I. Rehberg, Phys. Rev. E **64**, 041305 (2001).

[36] Y. Y. Villanueva, D. V. Denisov, S. de Man, and R. J. Wijngaarden, Phys. Rev. E **82**, 041303 (2010).

[37] D. V. Denisov, Y. Y. Villanueva, and R. J. Wijngaarden, Phys. Rev. E **83**, 061301 (2011).

[38] I. Zuriguel, J. F. Boudet, Y. Amarouchene, and H. Kellay, Phys. Rev. Lett. **95**, 258002 (2005).

[39] M. N. Bannerman, R. Sargant, and L. Lue, J. Comput. Chem. **32**, 3329 (2011).

[40] D. C. Rapaport, *The Art of Molecular Dynamics Simulation* (Cambridge University Press, Cambridge, UK, 2004).

[41] P. K. Haff, J. Fluid Mech. **134**, 401 (1983).

[42] J. Sack and J. Urrutia, *Handbook of Computational Geometry* (Elsevier Science, Amsterdam, 1999).

[43] I. Goldhirsch and G. Zanetti, Phys. Rev. Lett. **70**, 1619 (1993).

[44] T. Pöschel, N. V. Brilliantov, and T. Schwager, J. Phys.: Condens. Matter **17**, S2705 (2005).

[45] J.-P. Hansen and I. R. McDonald, *Theory of Simple Liquids* (Academic Press, San Diego, CA, 1990).

[46] H. Khalilian, M. R. Nejad, A. G. Moghaddam, and C. M. Rohwer, Europhys. Lett. **128**, 60006 (2020).

[47] Z. Jabeen, R. Rajesh, and P. Ray, Europhys. Lett. **89**, 34001 (2010).

[48] T. Schindler and M. Schmidt, J. Chem. Phys. **145**, 064506 (2016).